THE ASTROPHYSICAL JOURNAL, 279:633–649, 1984 April 15


# THE EVOLUTION OF STAR-BEARING MOLECULAR CLOUDS: THE HIGH-VELOCITY $HCO^+$ FLOW IN NGC 2071

ALWYN WOOTTEN,[1,2,3] ROBERT B. LOREN,[4] AAGE SANDQVIST,[5] PER FRIBERG,[6] AND ÅKE HJALMARSON[6]
*Received 1983 June 20; accepted 1983 September 27*

## ABSTRACT

The $J = 1$–0 and $J = 3$–2 lines of $HCO^+$ and $H^{13}CO^+$ have been observed in the molecular cloud NGC 2071, where they map the dense portions of a bidirectional molecular flow. The high resolution (42″) of our observations has enabled us to determine the distribution of mass, momentum, and energy in the flow as a function of projected distance from the cluster. Both momentum and energy diminish with distance from the central cluster of infrared sources. The highest velocities at a given intensity in this dense flow occur in a limited region coincident with an infrared cluster and the densest part of the molecular cloud. Higher resolution (33″) CO and $^{13}CO$ observations reveal that the extreme velocities in the flow occur in regions displaced on opposite sides of the cluster, suggesting that the flow only becomes visible in molecular line emission at distances $\sim 0.1$ pc from its supposed source. Lower velocity material containing most of the mass of the flow is found over larger regions, as expected if the flow has decelerated as it has evolved. Assuming conservation of momentum, the historical rate of momentum injection is found to have been roughly constant over a period of $10^4$ years, suggesting a constancy of the average luminosity of the central cluster over that time. The $J = 3$–2 $HCO^+$ profile does not show the absorption which is a prominent feature of the $J = 1$–0 profile, and the $J = 3$–2 line appears to be a useful probe of conditions specific to the dense cores of clouds. The high velocity $HCO^+$ emission correlates very well with spatial and velocity extents of molecular hydrogen emission. The abundance of $HCO^+$ [$X(HCO^+) \sim 10^{-8}$], and by inference the electron density, is similar in material at all velocities.

*Subject headings:* interstellar: molecules — nebulae: individual — stars: formation

## I. INTRODUCTION

Localized high-velocity gas in molecular clouds was first observed in the $J = 1$–0 line of $^{12}CO$ (hereafter CO) toward the infrared cluster embedded in the Orion molecular cloud (OMC-1) by Kwan and Scoville (1976) and Zuckerman, Kuiper, and Rodriguez-Kuiper (1976). High-velocity CO wings from molecular flows have subsequently been observed toward other active regions of star formation, notably Mon R2 (Loren 1977), L1551 (Snell, Loren, and Plambeck 1980), Cep A (Rodríguez, Ho, and Moran 1980), AFGL 490 (Lada and Harvey 1981), and NGC 2071 (Loren 1981*a*; Lichten 1982; Bally 1982). One intriguing aspect of these flows, discovered in L1551 by Snell, Loren, and Plambeck (1980) and subsequently recognized in other objects, is that the flow is channeled into oppositely directed lobes.

A key parameter leading to estimates of the momentum and energy of these flows is their mass. Unfortunately CO lines, which are bright and easily observed, are usually optically thick over much of their velocity extent (Loren *et al.* 1981; Plambeck, Snell and Loren 1983) and cannot be used to accurately determine the mass of the flow. Observations of $^{13}CO$ wing emission could accurately measure the mass of flow material, but these lines are very weak. $HCO^+$ wing emission, as we shall show, is not only bright but optically thin and excited only in dense regions. In order to investigate the physical parameters of the high-velocity gas, we have pursued an earlier observation (Loren and Wootten 1980) that the velocity extent of the wings on the $HCO^+$ line is similar to those observed in CO. Because of the quantity of data we have amassed, and because the complexities of each region require specific discussion, we report our observations in a series of papers, on NGC 2071 (this paper), Cep A (Loren *et al.* 1983), W3 (Sandqvist *et al.* 1982*a*, *b*), and OMC-1 (Wootten and Loren 1984).

The reflection nebula NGC 2071 and its associated H II region (Gilmore 1980) lie at a distance of $\sim 500$ pc (Strom, Strom, and Vrba 1975) in the opaque dust cloud L1630. Extensive surveys of CO and $^{13}CO$ (Loren 1981*a*; White and Phillips 1981) have revealed a dense region centered 3′ north of the nebula. In a survey of the complex at 2 μm Strom, Strom, and Vrba (1975) found a highly obscured star in the dense cloud near the position of a peculiar strong OH maser (OH 205.1 − 14.1, Johansson *et al.* 1974; Pankonin, Winnberg, and Booth 1977) and $H_2O$ maser sources (Campbell 1978; Genzel and Downes 1979). Subsequent observers (Evans *et al.* 1979; Harvey *et al.* 1979) have identified a bright 10 μm source (IRS 1), for which accurate positions have recently been measured by Allen, Barton, and Gillingham (1980) and Persson *et al.* (1981). Persson *et al.* found several additional but weaker 10 μm infrared sources clustered near IRS 1, and also detected high-velocity emission from molecular hydrogen. The nature of the cluster has been clarified by

[1] Department of Physics, Rensselaer Polytechnic Institute.
[2] Owens Valley Radio Observatory, California Institute of Technology.
[3] National Radio Astronomy Observatory, Charlottesville, Virginia.
[4] Millimeter Wave Observatory, McDonald Observatory; and Electrical Engineering Research Laboratory, The University of Texas at Austin.
[5] Stockholm Observatory, Saltsjobaden, Sweden.
[6] Onsala Space Observatory, Onsala, Sweden.

far-infrared measurements of its spectrum. Harvey *et al.* (1979) measured the integrated far-infrared luminosity toward the cluster, unresolved in their 40″ beam, to be $\sim 750\ L_\odot$, a luminosity similar to that of a single B5 star. More extensive far-infrared maps (Sargent *et al.* 1981) measure a luminosity of $\sim 1000\ L_\odot$ at IRS 1, which might be provided by a B3 star, and $\sim 3000\ L_\odot$ at NGC 2071 (H II), 3′ to the south. Sargent *et al.* suggest that the region near IRS 1 is much less evolved than that near NGC 2071 (H II).

Lada (1976) noted that the $J = 1$–0 CO line profiles toward NGC 2071 were self-absorbed with an unusual velocity structure which might indicate expansion of the absorbing layer. Loren and Wootten (1980) showed that the $J = 1$–0 $HCO^+$ profile was very similar to the CO profile. Loren *et al.* (1981) and Loren (1981*b*) illustrated the presence of broad CO wings, which have been traced to a 70 km s$^{-1}$ extent in a low noise spectrum by Bally (1982). The spatial distribution of the integrated flux in the red- and blueshifted CO wings (Bally 1982; Lichten 1982) disclosed a double lobed structure similar to that found in L1551 (Snell, Loren, and Plambeck 1980).

The measurements reported here include the $J = 1$–0 and $J = 3$–2 lines of the abundant $H^{12}CO^+$ species (hereafter $HCO^+$) as well as the same transitions of the scarce $H^{13}CO^+$ species. We report the first detection of the $J = 3$–2 line of $H^{13}CO^+$. We also have observed the $J = 1$–0 line of CO and $^{13}CO$ with 33″ resolution toward the cluster. The $HCO^+$ spectra exhibit a prominent narrow self-absorption in the $J = 1$–0 line but not the $J = 3$–2 line, and broad wings in both the $J = 1$–0 and $J = 3$–2 lines. In the following discussion we detail the spatial distribution of these features to determine the structure of the dense core of the cloud and the motions of gas through this region. The relationship of the gas producing $HCO^+$ emission to other molecular emission lines is also discussed.

## II. OBSERVATIONS

Observations have been made of two lines of $HCO^+$: the $J = 1$–0 line at 89.188523 GHz and the $J = 3$–2 line at 267.557619 GHz (Sastry, Herbs, and DeLucia 1981). The same transitions of $H^{13}CO^+$ at 86.754330 and 260.25540 GHz were also observed. The $J = 1$–0 lines were measured with the NRAO[7] 11 m antenna at Kitt Peak during 1980 June. The beamwidth of 75″ at 89 GHz is well matched to the beamwidth of the MWO telescope, 72″, measured at the higher frequency transitions and discussed below. Velocity resolutions of 0.34 and 0.84 km s$^{-1}$ were obtained with two 256-channel filter banks with 100 kHz resolution at the $HCO^+$ frequency. Calibration at NRAO was achieved by synchronous detection of an absorber vane. The temperature scale was confirmed through observations of S140 and M17 SW with an image sideband rejection filter installed at the beginning of the observing session. The forward spillover and scattering efficiency $\eta_{\rm fss}$ (Kutner and Ulich 1981) is 0.79; following their convention all intensities are expressed as $T_R^* = T_A^*/\eta_{\rm fss}$ or as $T_R = T_R^*/\eta_c$, where the coupling efficiency is chosen to be appropriate for a source of 2′ extent, $\eta_c = 0.81$ (Ulich and Haas 1976).

To obtain higher spatial resolution of the core region, the $J = 1$–0 lines of $HCO^+$, $H^{13}CO^+$, CO, and $^{13}CO$ were observed with the Onsala Space Observatory (OSO)[8] 20 m millimeter wave antenna. The beamwidth at 89 GHz is 42″, and at 115 GHz it is 33″. For this telescope the measured efficiencies are $\eta_{\rm fss} = 0.6$ and $\eta_c = 0.76$ or 0.59 for a 2′ source at 89 and 115 GHz, respectively. Cooled single-sideband tuned receivers with noise temperature 350 K were employed at each frequency, and calibration was achieved utilizing an absorber vane. An autocorrelation spectrometer achieved velocity resolutions of 0.2 km s$^{-1}$ during $HCO^+$ observations in 1980 March. In 1981 May, a filter bank spectrometer provided 256 channels of 250 kHz (0.84 km s$^{-1}$ for $HCO^+$) resolution, and the resolution of the autocorrelator was 0.1 km s$^{-1}$. In 1983 January the resolution at the CO line was 0.65 km s$^{-1}$ in the 250 kHz filter bank and 0.08 km s$^{-1}$ in the autocorrelator.

The $J = 3$–2 transitions of $HCO^+$ and $H^{13}CO^+$ were observed with the 4.9 m Millimeter Wave Observatory[9] (MWO) antenna. A 72″ beamwidth was measured, and the forward spillover and scattering efficiency was 0.83. Maps of the beam (Mundy 1982) and of the antenna surface (Mayer *et al.* 1983) indicate that the coupling efficiency $\eta_c$ is 0.63 for a uniform source of 2′ diameter. Observations during 1980 March were made with an uncooled receiver having a system temperature of 6000 K while observations during 1981 March and April and 1982 January used a cooled version of the same receier, which achieved a system temperature of 3000 K at 267 GHz. Calibration was obtained by synchronous detection of an ambient temperature absorbed to the sky. Two 128-channel filter banks provided velocity resolutions of 0.28 km s$^{-1}$ and 1.12 km s$^{-1}$.

The temperature scales of the $J = 1$–0 data were compared by observing the same source position at NRAO and OSO during periods of low sky opacity. The weather at OSO was exceptionally good during 1980 March, and the scales of the peak intensity of the $HCO^+$ line agree well. Maps of the sources, however, indicate that the wings of the $HCO^+$ line are relatively stronger in the OSO data. We attribute this mainly to the small size of the high-velocity source, but differences in the error patterns of the two antennas may also appear.

## III. RESULTS

### *a) The J = 1–0 Lines of* $HCO^+$

#### i) *The Line Profile at the Cluster*

In Figure 1*a*, the NRAO spectra of the $J = 1$–0 lines of $HCO^+$ and $H^{13}CO^+$ observed toward the NGC 2071 infrared cluster are shown superposed. The line shapes differ greatly. The wings on the $HCO^+$ line are quite apparent. Near line center, a very narrow (0.7 km s$^{-1}$) drop in line intensity occurs at $V_{\rm LSR} = 10$ km s$^{-1}$, which is visible over much of the source. The line is weaker on the negative

[7] The National Radio Astronomy Observatory (NRAO) is operated by Associated Universities, Inc., under contract with the National Science Foundation.

[8] Onsala Space Observatory, Chalmers University of Technology, is operated with financial support from the Swedish Natural Science Research Council. The receiver development has been sponsored by the Swedish Board for Technical Development.

[9] The MWO is operated by the Electrical Engineering Research Laboratory, The University of Texas at Austin, with support from the National Science Foundation and McDonald Observatory.

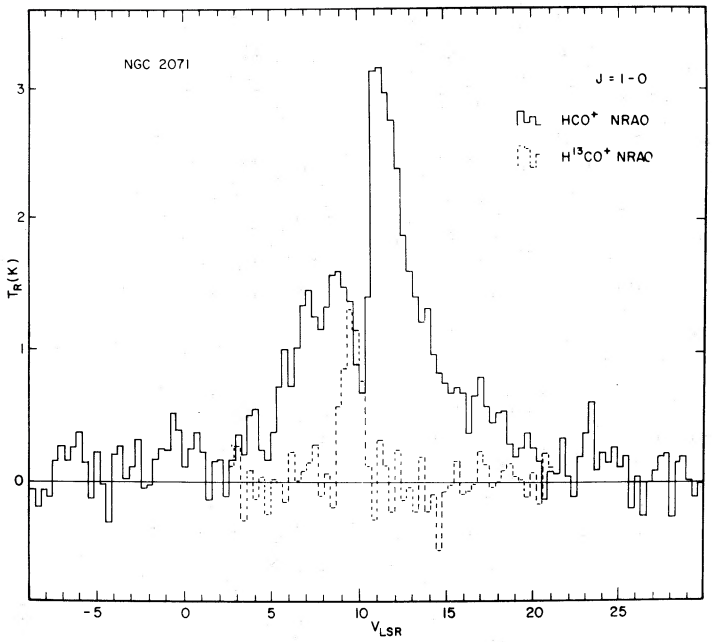


FIG. 1a

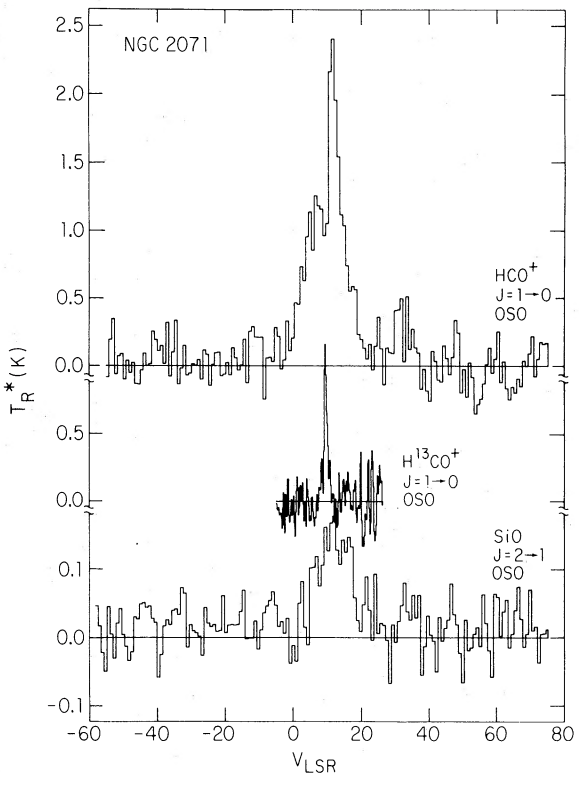


FIG. 1b

FIG. 1.—(*a*) Profiles of the $J = 1$–0 lines of $HCO^+$ and $H^{13}CO^+$ toward the position $\alpha = 05^h44^m30^s$, $\delta = 00°20'40''$, showing the self-absorption features and the prominent wings on the $HCO^+$ line. These data were taken with the NRAO telescope. (*b*) Profiles of the $J = 1$–0 lines of $HCO^+$ and $H^{13}CO^+$ taken with the OSO telescope at the position $\alpha = 05^h44^m30^s$, $\delta = 00°20'40''$. The lowermost spectrum is the $J = 2$–1 SiO line observed by Olofsson *et al.* (1982*b*).

velocity side of this dip in the profile. In Figure 1*b* the OSO spectra of three lines are shown. The $J = 1$–0 $HCO^+$ line has relatively stronger wings when observed with the smaller beam of this telescope, extending over a velocity interval of 25 km $s^{-1}$, but no structure is apparent in the $H^{13}CO^+$ line. The lowermost spectrum is the $J = 2$–1 SiO line observed by Olofsson *et al.* (1982*b*) which occurs at an unusual velocity ($\sim 12$ km $s^{-1}$), is of intermediate breadth (18 km $s^{-1}$), and arises in an unresolved ($< 44''$) region.

ii) *Spatial Distribution of Line Emission*

The spatial extent of the core is shown by the distribution of peak intensity in the $J = 1$–0 line of $HCO^+$, Figure 2. The full width to half-maximum intensity of the core is 90″. The map is somewhat asymmetric, an artifact of the absorption of radiation from the core by a low excitation (cooler) portion of the complex centered to the northeast, as will be evident from a comparison between the $J = 1$–0 and $J = 3$–2 spectra discussed in § III*c*(i). As a result, the centroid of the map is shifted to the southwest, and the apparent shape of the core is elongated, mimicking the form a disk might take. The structure of the core does not appear disklike on small scales, as will be discussed in § V.

Unaffected by foreground gas, the optically thin $H^{13}CO^+$ line (Fig. 1) should accurately reflect the mass distribution along the line of sight. A small OSO map in this line indicates that the mass is concentrated to the region of the infrared cluster.

iii) *Velocity Distribution of Line Emission*

In Figures 3 and 4, a series of maps of NGC 2071 show the distribution of molecular emission as a function of $V_{LSR}$. Figure 3 shows a velocity-position map along a northeast-southwest line through the infrared cluster. Figure 4*a* shows emission integrated over a velocity range $-13$ to $-8.8$ km $s^{-1}$. At this velocity, the source appears unresolved in the Onsala 42″ beam (i.e., $< 0.1$ pc) and is located at the position of the 10 $\mu$m cluster. This behavior is followed by emission in the range $-8.8$ to $-4.6$ km $s^{-1}$, illustrated in Figure 4*b*. At the velocities of Figure 4*c*, $-4.6$ to $-0.4$ km $s^{-1}$, the source appears to be distributed over a somewhat larger area, but the most intense emission still occurs near the cluster. The intermediate velocities of Figure 4*d*, $-0.4$ to $+3.8$ km $s^{-1}$, show a clearly resolved source extending to the northeast. The map resembles that of the blue lobe of CO emission (Bally 1982), but peak intensity occurs near the cluster. The blue lobe is well developed in Figure 4*e*, 3.8–8.0 km $s^{-1}$, and extends to the limits of our map. Significantly, the spatial extent of the lobe in this panel resembles that of the broad self-absorption feature. Figure 4*f* shows the emission in the line core. The red lobe, at velocities 12.2–16.4 km $s^{-1}$, extends to the southwest in Figure 4*g*, diametrically opposite

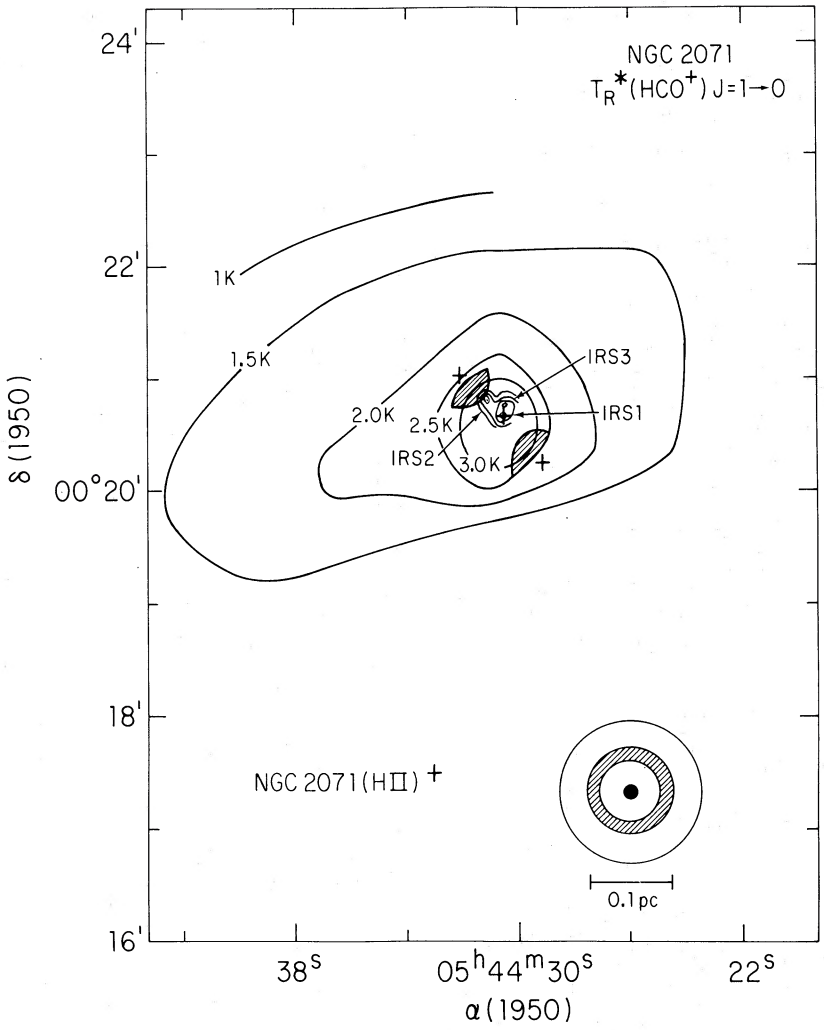


FIG. 2.—A map of the $J = 1$–0 $HCO^+$ emission from the NGC 2071 molecular cloud. Also shown are the 10 $\mu$m map of Persson *et al.* (1981) and the location of the H II region from Gilmore (1980). Both IRS 1 and IRS 3 also coincide with radio sources (Bally and Predmore 1983). The positions of the CO data are shown with + signs, and the beam sizes are given in the lower right: from smallest to largest they are $H_2$ (Persson *et al.* 1981), CO (OSO), $HCO^+$ (OSO), and $HCO^+$ (NRAO, MWO). Regions of overlap of the OSO and OVRO CO beams are shown by cross-hatching. Some of the highest velocity CO emission arises in these regions.

to the blueshifted lobe. Comparison of Figures 4*e* and 4*g* illustrates the bipolar aspect of the velocity field. The source is barely resolved at velocities of 16.4–20.6 km $s^{-1}$ (Fig. 4*h*), once more peaking on the infrared cluster. By the final panel, (4*i*), showing a velocity range of 20.6–24.9 km $s^{-1}$, the source has again become unresolved, and the only detectable emission is coincident with the infrared cluster.

These panels illustrate several interesting features of the velocity field. First, at any velocity, the maximum $HCO^+$ intensity occurs within the beam centered on the infrared cluster. Second, the bipolar nature of the flow is *only* apparent at intermediate velocities, where the source is resolved. Finally, at the highest velocities, the source is unresolved and coincident with the infrared cluster. Unfortunately, the wing intensity drops so rapidly at high velocities that we were unable to detect any high-velocity emission despite a long integration at a position 30″ S of the cluster. We conclude that although some high-velocity emission may be present at positions away from the cluster, only a small part of the mass in the flow can be contained in that component.

iv) *The* $H^{13}CO^+$ *Line*

No wings are visible in the weak $H^{13}CO^+$ line (Fig. 1). Because of its low optical depth, this line is useful for the determination of the velocity of the densest part of the core. Perpendicular to the axis defined by the bipolar flow, from northwest to southeast across the infrared cluster, the velocity of $H^{13}CO^+$ line center shifts redward by 0.8 km $s^{-1}$. Remarkably, this change occurs abruptly in an unresolved region near the cluster (Fig. 5). A velocity gradient has previously been observed over a larger region of the core in $^{13}CO$ emission by Lichten (1982) and in CS by Bally (1982). Lichten's observations have higher resolution, and confirm

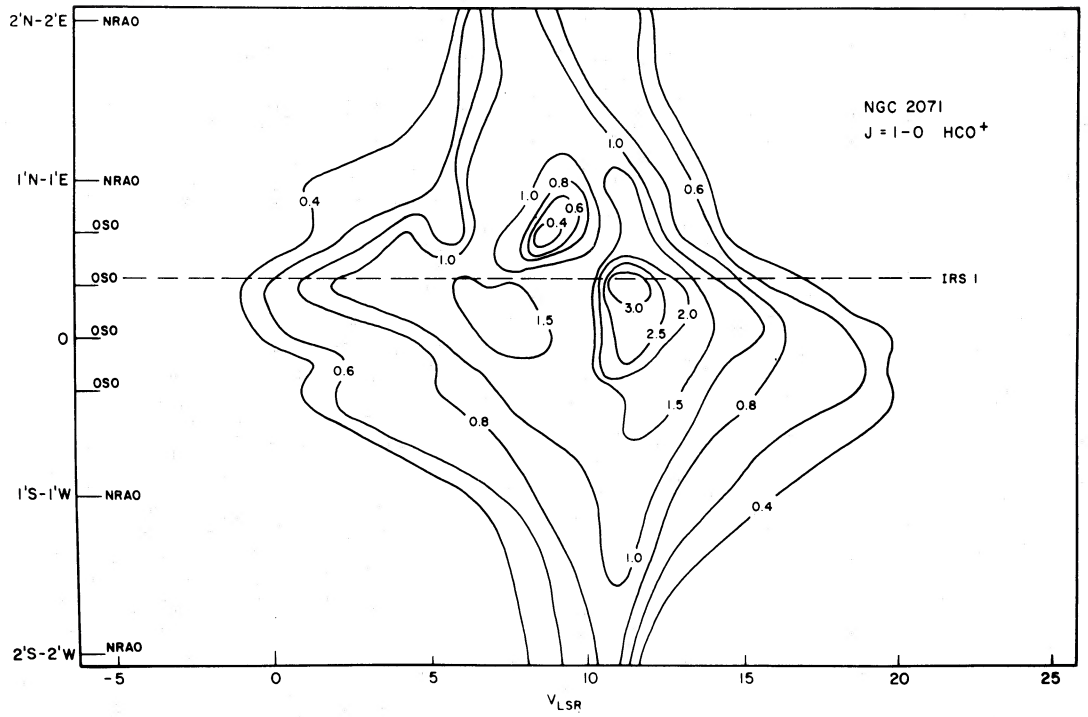


FIG. 3.—A map of $HCO^+$ ($J = 1$–0) emission along a northeast-southwest axis passing 20″ south of IRS 1 (position 0). The smallest distance between beam center and IRS 1 occurs at the position shown as a dashed line. The map was constructed by hybridizing OSO and NRAO data taken at positions labeled along the ordinate.

that part of the velocity shift occurs in a small region near the infrared cluster. On an even larger scale, White and Phillips (1981) have found a velocity gradient in the $J = 1$–0 CO emission.

### b) *The* $J = 1$–0 *Lines of* CO

There are some important differences between the $HCO^+$ observations, which sample a very dense component of the flow, and the CO observations, which are also sensitive to less dense components of the flow. Bally (1982) measured the full width of the $J = 1$–0 CO line to be 70 km $s^{-1}$ at a 50 mK level with the 1.′7 beam of the Bell Telephone Laboratories (BTL) telescope centered on IRS 1. We have measured a similar width (75 km $s^{-1}$) in a spectrum (Fig. 6) obtained with the 0.′9 beam of an Owens Valley Radio Observatory (OVRO) telescope (Lichten 1983). In contrast, the CO spectrum obtained with the 0.′55 beam of the OSO telescope has a full width of only 35 km $s^{-1}$ (Fig. 6), while OSO spectra taken at nearby positions (Fig. 6) show that *the extreme velocities in the large beam* CO *profiles originate in spatially separate parts of the cloud.*

Other OSO spectra in Figure 6 were taken one full beam northeast and southwest ($(\Delta\alpha, \Delta\delta) = (23'', 23'')$ and $(-23'', -23'')$) of IRS 1. These spectra evidently begin to resolve the structure of the highest velocity material. Clearly, the bluest emission visible in the OVRO or BTL spectra is present only in the vicinity of the northeast spectrum, and the reddest emission in those spectra is strongest in the vicinity of the southwest spectrum. The highest velocity blue emission is stronger in the OVRO spectrum than in the BTL spectrum by a factor equal to the ratio of beam areas, indicating that the source is smaller than 1′. The emission intensity at these highest velocities does not increase by more than an additional 30% when observed with the OSO beam, and so the emitting region does not lie entirely within that beam. The region of overlap between the OVRO and OSO beams is marked in Figure 2, and lies just northeast of IRS 2 and IRS 4. In contrast, the region from which the stronger red emission arises lies southwest of IRS 1. In both cases the highest velocity CO emission lies *outside the region defined by the* 10 $\mu$m *cluster*. This contrasts with the $HCO^+$ and SiO emission, as we have seen, and the $^{13}CO$ emission (Fig. 6), all three of which have much smaller velocity extents (20–25 km $s^{-1}$). For all of these molecules, the highest velocity emission we have detected lies within the region defined by the 10 $\mu$m cluster to within our resolution. CO emission is strong over the entire velocity extent of emission from either of these molecules. We conclude that the very highest velocity CO component is not sufficiently massive to emit detectable $^{13}CO$ or $HCO^+$ emission. The appearance of highest velocity emission in this component exterior to the cluster suggests that this component may be driven by the combined forces of the embedded cluster members.

### c) *The* $J = 3$–2 *Lines of* $HCO^+$

#### i) *Line Profiles*

In marked contrast to the $J = 1$–0 $HCO^+$ profile of Figure 1, the $J = 3$–2 $HCO^+$ lines (Fig. 7) show no evidence for self-

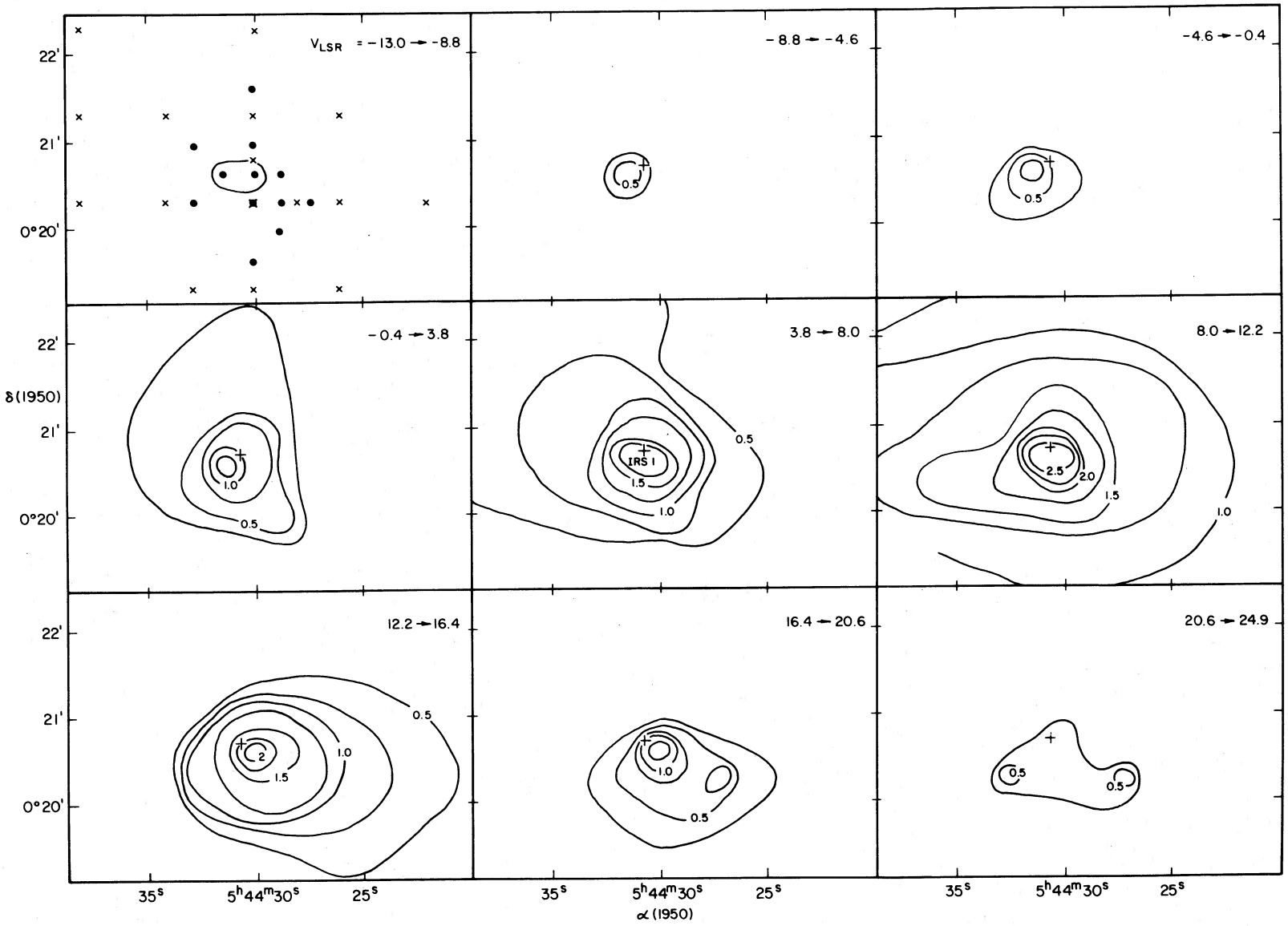


FIG. 4.—Maps of $HCO^+$ emission in various velocity intervals in the region of the NGC 2071 infrared cluster. Panels are ordered from the upper left in rows according to increasing velocity. (*a*) The range $-13 < V_{LSR} < -9$ km s$^{-1}$ shows that emission is unresolved by the OSO beam at velocities 20 km s$^{-1}$ blueward of line center and is centered near IRS 1 (*plus sign* in subsequent panels). Both OSO (*filled circle* position) and NRAO (*cross* positions) data have been used to construct these maps. (*b*) The emission region remains unresolved at velocities near 16 km s$^{-1}$ shortward of line center. (*c*) Resolution of the emission region is achieved at velocities 12 km s$^{-1}$ shortward of line center. (*d*) The extensive short-wavelength emission lobe extending to the northeast is apparent at 8 km s$^{-1}$ from line center. (*e*) The short-wavelength lobe is fully developed and not completely mapped at velocities near 4 km s$^{-1}$ shortward of line center. (*f*) Emission at the line core centers on the young cluster. (*g*) Longward of line center by 4 km s$^{-1}$ the long-wavelength lobe extends to the southwest. (*h*) The extent of the long-wavelength lobe shrinks near 8 km s$^{-1}$ from line center, and by (*i*) the long-wavelength lobe is again unresolved, 12 km s$^{-1}$ from line center.

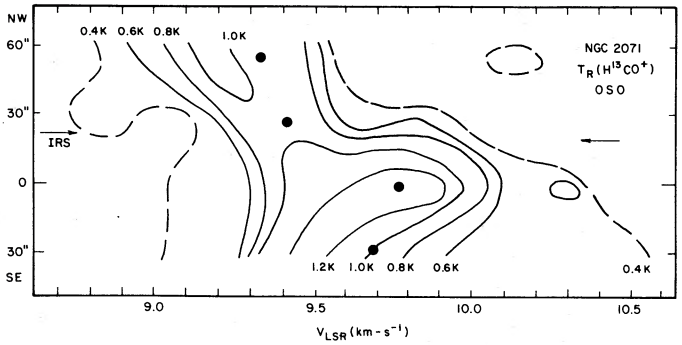


FIG. 5.—Velocities of $J = 1$–0 $H^{13}CO^+$ along a northwest-southeast line passing 20″ south of the infrared cluster, orthogonal to the map in Fig. 3. Note that the velocity of the $J = 3$–2 $HCO^+$ occurs at 9.6 km s$^{-1}$, while the $J = 2$–1 CS line (Bally 1982) and the $J = 1$–0 CO and $HCO^+$ lines peak above 10 km s$^{-1}$ owing to the effects of foreground absorbing material.

reversal. The $J = 3$–2 line of both isotopic species peaks near 9 km s$^{-1}$, blueward of the narrow self-absorption dip on the $J = 1$–0 profile, and at the peak velocity of the $J = 1$–0 $H^{13}CO^+$ line. The absorbing cloud apparently has little effect on $J = 3$–2 photons, although from the intensity and breadth of the line one infers that it has substantial opacity. $HCO^+$ molecules in the absorbing cloud are probably not appreciably excited to levels as high as $J = 2$, as this cloud is most likely of low density (Lichten 1982).

ii) *Spatial Distribution of Line Emission*

The $J = 3$–2 line, requiring high density for excitation, arises in an extended region of size 90″, shown in Figure 8.

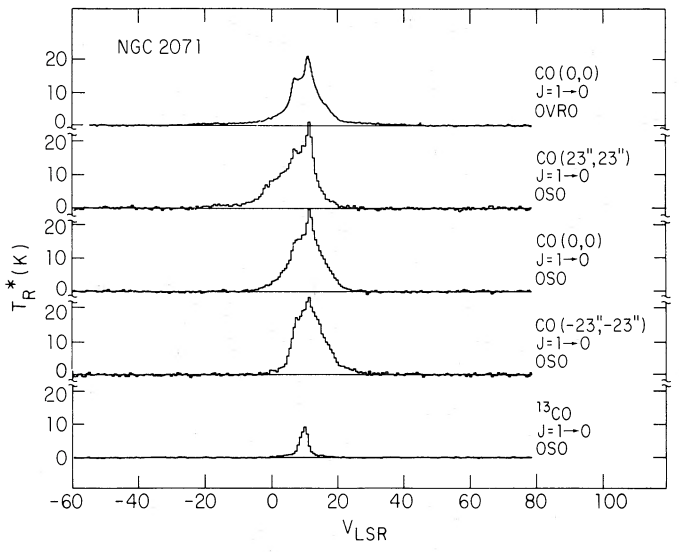


FIG. 6.—CO spectra toward the infrared cluster in NGC 2071 and nearby regions. The uppermost spectrum is the OVRO CO spectrum (Lichten 1982). The next three lower spectra are OSO spectra at positions $(\Delta\alpha, \Delta\delta) = (23'', 23'')$, $(0'', 0'')$, and $(-23'', -23'')$ relative to IRS 1. The lower spectrum is a $^{13}CO$ spectrum taken at OSO toward IRS 1. A $^{13}CO$ spectrum taken at $(\Delta\alpha, \Delta\delta) = (23'', 23'')$ is identical to within the uncertainties. The upper OSO spectrum, showing a strong blue wing, was obtained near IRS 2. An $H_2$ spectrum (Persson *et al.* 1981) obtained here also shows strong blue wings and little emission redward of peak intensity.

Although the $J = 3$–2 and $J = 1$–0 emission regions are comparable in spatial extent, the former is more symmetric about the position of the infrared cluster, where it peaks. This behavior confirms our contention that the absorbing cloud shifts the apparent centroid of the $J = 1$–0 map and flattens its appearance, causing it to resemble a tilted disk.

iii) *Velocity Distribution of Line Emission*

It is difficult to reach sufficient sensitivity at 267 GHz to map weak emission such as that found in line wings. Line wings are present in the central position to $\pm 7$ km s$^{-1}$ at the 3 sigma level in one 1 MHz channel. At velocities $V_w$ above 5 km s$^{-1}$ from line center (taken to be 9.8 km s$^{-1}$), blue and red wings are of similar intensity, although in the interval 1 km s$^{-1}$ $< V_{LSR} <$ 5 km s$^{-1}$ the shortward wing is stronger by an average factor of 2. At positions away from the infrared cluster, the highest velocity $HCO^+$ weakens below detectability, also a feature of the $J = 1$–0 $HCO^+$ data discussed earlier. To the southwest, the wings are present at the three sigma level to $\pm 5$ km s$^{-1}$, and to the northeast they are present to $\pm 4$ km s$^{-1}$. While in the southwest the ratio of blue to red wing intensity (1 km s$^{-1}$ $< V_{LSR} <$ 5 km s$^{-1}$) is similar to but slightly less than at center ($2.01 \pm 0.07$), the blue wing is stronger relative to the red ($3.5 \pm 0.31$) to the northeast. This pattern is also in agreement with that found in the $J = 1$–0 line, where at intermediate velocities the emission contours define a "blue lobe" to the northeast and a "red lobe" to the southwest. The and a "red lobe" to the southwest. The intensity ratio in the wings between the $J = 3$–2 and $J = 1$–0 lines is near unity at all positions.

Since the central velocity of the $J = 3$–2 line is not shifted by foreground absorption, it accurately measures the center of rest velocity of the dense gas. As in the $^{13}CO$ and $H^{13}CO^+$ lines, there is evidence for an increase of the velocity of line center from northwest to southeast across the cluster, but our map is neither extensive enough nor of high enough spectral resolution to measure the gradient.

The $J = 3$–2 $H^{13}CO^+$ (Fig. 7) profile resembles the $J = 1$–0 $H^{13}CO^+$ profile in its shape and central velocity.

## IV. STRUCTURE AND ENERGETICS OF THE FLOW

To characterize the source of the flow in NGC 2071, it will be useful to determine the mass, energy, and momentum in the flow and to determine its ionization state. Direct measurement of these quantities might be obtained from observations at 2 $\mu$m of molecular hydrogen emission. Unfortunately, the $H_2$ lines are difficult to detect, they are attenuated to an unknown degree by interstellar absorption, and they are excited only in regions of high density and temperature. Indirect estimates of mass, energy, and momentum in the flow from trace constituents such as $HCO^+$ and CO require a knowledge of the abundance, $X$, of these molecules relative to molecular hydrogen. This is particularly important in a region where shocks may alter the chemical composition of the flow from that in the ambient interstellar gas.

The measurement of molecular abundances requires a knowledge of the optical depth of the optically thin emission from the molecule. The intensity ratio of two different transitions of the molecule over velocity ranges where the

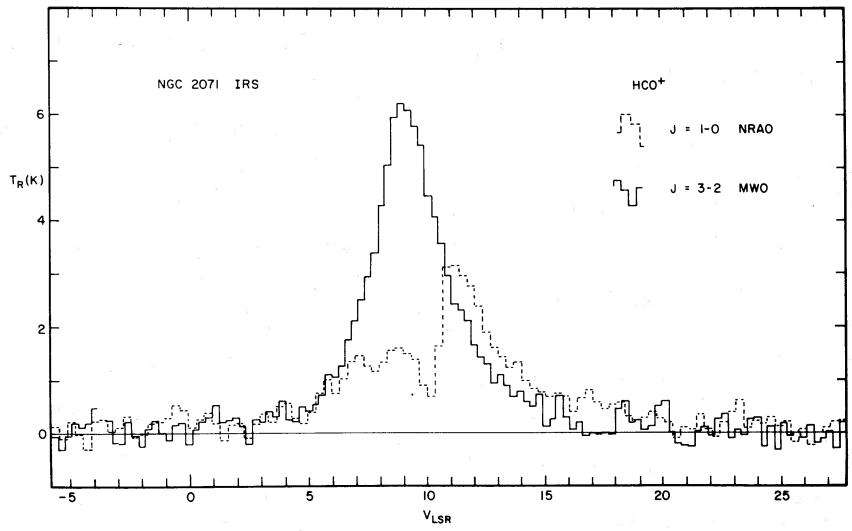


FIG. 7*a*

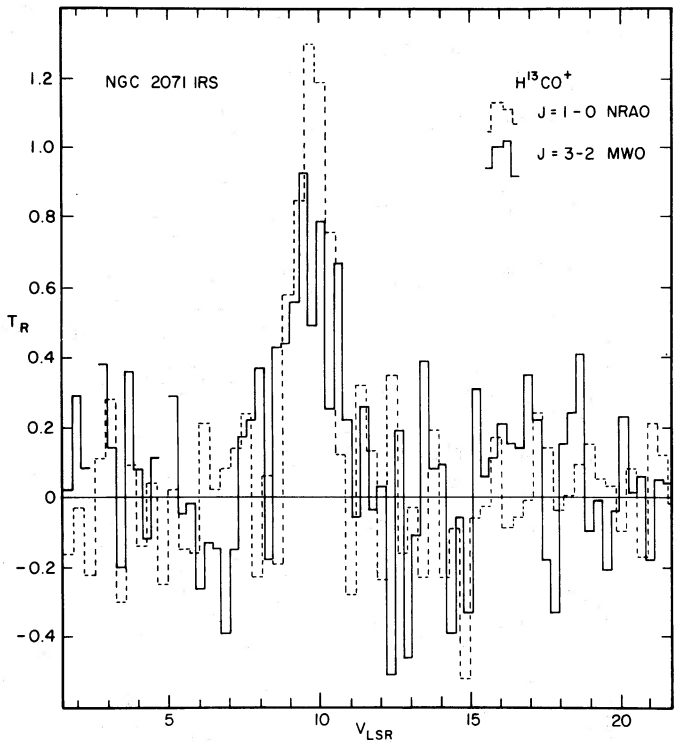


FIG. 7*b*

FIG. 7.—Profiles of the $J = 1$–0 (NRAO) and the $J = 3$–2 (MWO) lines of $HCO^+$ and $H^{13}CO^+$ observed toward the infrared cluster. Note particularly the absence of self-absorption in the latter line and its extensive wings.

emission is thick and thermalized will vary little from unity (eq. [A9]). Over velocity ranges where emission is thin, the intensity ratio will vary with the optical depths of the lines (eq. [A8]). For many molecules, emission in the line cores of two transitions may be optically thick while emission in the wings may be thin. The ratio of the two lines will then show a characteristic variation with velocity, reflecting these regimes. A similar situation occurs if profiles of the same transition of isotopic variants of a molecule are compared. Loren *et al.* (1981) measured the intensities of the $J = 1$–0 and $J = 2$–1 lines of CO in NGC 2071 and found a nearly constant intensity ratio ($\sim 1.2$) across the central 18 km $s^{-1}$ of the line profiles, which suggests the emission is optically thick over this velocity range. Figure 9*a* shows the ratio of the $J = 1$–0 line of CO to the $J = 1$–0 line of $^{13}CO$. This ratio varies considerably with velocity, but it approaches

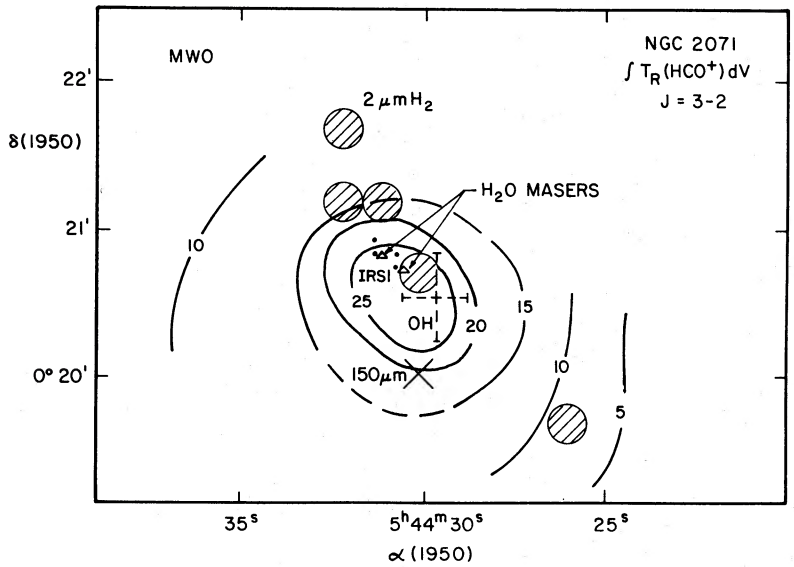


FIG. 8.—A temperature map showing the extent of emission in the $J = 3$–2 line of $HCO^+$. The infrared sources mapped by Persson *et al.* (1981) are located at the filled circles. The open triangles locate an $H_2O$ maser, and the dashed cross locates the OH maser. Hatched circles trace the region where the $H_2$ emission was found by Bally and Lane (1982). The 20 K km s$^{-1}$ contour approximates the MWO beam size.

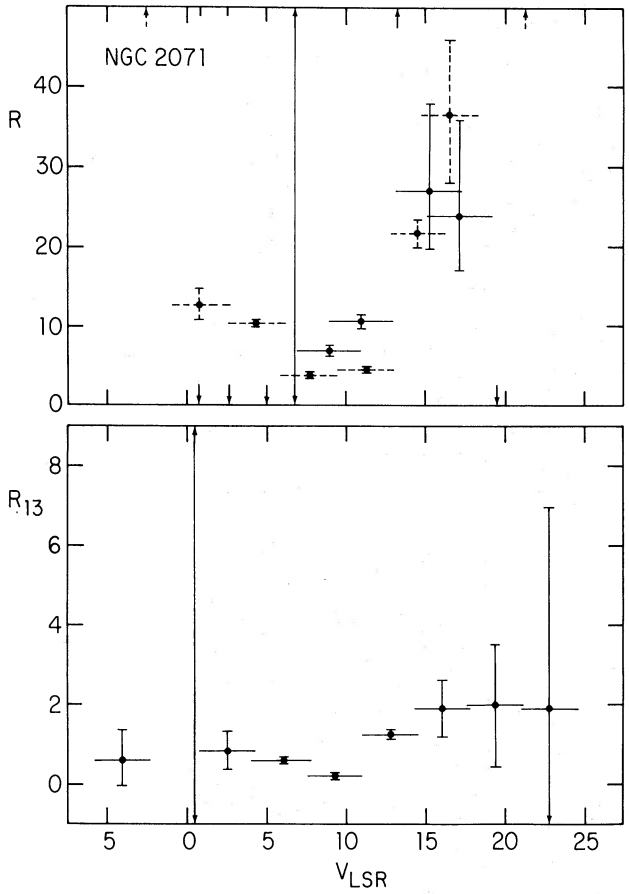


FIG. 9.—*Top*, the intensity ratio of $J = 1$–0 $HCO^+$ to $H^{13}CO^+$ (OSO) lines is shown by a solid line, and the intensity ratio of J = 1–0 CO to $^{13}CO$ (OSO) is shown with dashed lines. *Bottom*, the intensity ratio $R_{13}(v)$, defined in the text, is plotted as a function of velocity. The shape of this curve resembles those in panel a of this figure.

the C/$^{13}$C isotope ratio only at the highest velocities. From these data we conclude that the CO transitions are optically thick over much of the line core (Plambeck, Snell, and Loren 1983 measure $\tau \sim 2$ at $V_{LSR} = 5$ and 17 km s$^{-1}$). Emission by $^{13}CO$, however, is thick over a velocity range which is much more restricted. For comparison, the $HCO^+/H^{13}CO^+$ ratio is also plotted in Figure 9*a*. At velocities within $\sim 3$ km s$^{-1}$ of line center the ratio is $7 \pm 0.6$, increasing above 15 at larger velocity displacements. The CO to $^{13}CO$ emission ratio is smaller than this. We believe that these isotopic ratios, and the fact that the $HCO^+/^{13}CO$ ratio increases in the line wings and is always greater than 2, indicate that the optical depth in the $HCO^+$ line wings is not large.

Our conclusion is reinforced by the ratio of the two $HCO^+$ transitions, $R_{13}(v) = T_{R,J=1-0}(v)/T_{R,J=3-2}(v)$, shown in Figure 9*b*. For these data, taken with the same beamsizes, $R_{13}(V_w > 5)$ falls in the range 0.5–2. Because the Rayleigh-Jeans approximation defining $T_R$* underestimates line intensities by differing amounts at 267 and 89 GHz, the intensity ratio for optically thick lines as we have defined it is a function of excitation temperature. However, $R_{13}(V_w)$ exceeds 0.85 for excitation temperatures which are above 2.5 K and equal in the two lines. We believe that the variation in the intensity ratio in Figure 9*b*, similar to the variations in isotope ratios in Figure 9*a*, indicates relatively low optical depths in the $HCO^+$ line wings. Because of the lower degeneracy of the lower rotational levels, the $J = 1$–0 line is of intrinsically lower optical depth than the $J = 3$–2 line in the high-velocity material, and we conclude that the optical depth in the $J = 1$–0 line wings is low.

To interpret the line ratio $R_{13}(V_w)$ in Figure 9*b*, we refer to the radiative transfer calculations using a large velocity gradient (LVG) code illustrated by Loren, Wootten, and Peters (1984). These calculations trace the behavior of the $J = 3$–2 to $J = 1$–0 line ratio as a function of abundance,

temperature, and density. Ratios above 1 can occur in optically thin material of densities in the range $n(H_2) \sim 4 \times 10^5$ to $10^6$ cm$^{-3}$. Unfortunately, the intensity ratio is not sensitive to abundance in this density regime—the absolute intensity of one of the lines must also be known.

The emission observed probably arises in small clumps and the emergent intensity is diluted by the beam size, rendering it useless for a direct abundance determination. Comparison of the OSO and NRAO data illustrates this. The intensity in the line wings increases with decreasing beam size at the central position. If the line wing results from a superposition of emission from many dense but small clumps of gas, this observation suggests that the clumps concentrate to the cloud core. The maps of Figure 4 also constitute evidence that the high-velocity emission is beam-diluted because the source appears smaller as it is viewed at higher velocities. Furthermore, Bally (1982) has argued that CO wing emission arises in many unresolved clumps, reasoning that the CO emission must be optically thick if $^{13}$CO emission is observed, so that the weak intensity at all velocities in the line wing probably reflects beam dilution rather than (*a*) weak excitation in low-density gas, which is ruled out by the $HCO^+$ observations, or (*b*) intrinsically low optical depth, which is ruled out by observations of the ratio of the $J = 2$–1 to $J = 1$–0 transition of CO (Loren *et al.* 1981). From the line intensity predictions of the LVG model ($T_R > 10$ K) and the observed wing intensity ($T_R > 0.1$ K) we estimate a surface filling factor in an approximate range of 0.01–0.05.

We therefore conclude that, while the value of $R_{13}(V_w)$ fixes the density of the emitting gas and is evidence for a moderate optical depth in the line wing, it fails to measure the $HCO^+$ abundance.

Ideally, the abundance of $HCO^+$ in the high-velocity gas should be determined from comparison to optically thin emission from a molecule of similar excitation requirements. Lacking such data, comparison can be made with the $^{13}$CO line. A similar comparison forms the basis for a measurement of the $HCO^+$ abundance in the high-velocity gas in OMC-1 (Kuiper, Zuckerman, and Rodríguez Kuiper 1981). Assuming that at each velocity emission from $^{13}$CO and $HCO^+$ molecules subtends a similar fraction $f$ of the beam solid angle, then $T_R^*(v) = f\tau(v)T_{ex}$, where $\tau(v)$ is the line optical depth at a velocity $v$ and $T_{ex}$ is the excitation temperature of the emitting material, assumed equal for the two molecules. The ratio of line intensities is then the ratio of optical depths in the line, which in turn yields the ratio of column densities for the two molecules. Far-infrared measurements determine the dust temperature in the core to be 40–42 K (Sargent *et al.* 1981; Harvey *et al.* 1979), and the CO measurements of Phillips *et al.* (1981) place the gas kinetic temperature at 34 K. The gas and dust temperatures are therefore well coupled in the dense core, and we may safely assume $T_{ex} = 35$ K in that region. Selecting $V_{LSR} = 17$ km s$^{-1}$, we find $X(HCO^+)/X(^{13}CO) = 0.014$, essentially the same as the value of 0.01 found for the OMC-1 high-velocity gas near the BN/KL region determined by Kuiper, Zuckerman, and Rodríguez Kuiper (1981). If one takes $X(^{13}CO) = 10^{-6}$, then $X(HCO^+) = 10^{-8}$, similar to that found in the OMC-1 flow near BN/KL but higher than the abundance found in cloud cores by Wootten, Snell, and Evans (1980). Note that this abundance and the measured line width combine to provide an estimate of the abundance-velocity gradient parameter $X/(dv/dr)$ which is consistent with the LVG model discussed above. We will return to a discussion of comparative abundance later (§ VI).

Before proceeding to calculate the mass, energy, and momentum in the flow, we separate the flow into several zones suggested by the data in Figure 4. Since the size of the source is a function of velocity, we define a characteristic radius for each velocity in the flow. At each velocity $v$, the area over which $T_R(v) > 0.2$ K, summed over a 4.2 km s$^{-1}$ bin, is measured. The geometry of the volume whose surface we observe is unknown. The bipolarity of the flow suggests a roughly conical geometry for each lobe (Barral and Cantó 1981), but the opening angle of such a cone is as yet uncertain. For opening angles between 30° and 70° the height of the cone and the radius of a sphere of the same projected area differ only by a factor of about 2. Let us then define for this region a characteristic radius, $r_c$, of the flow at velocity $V_w$ from the rest velocity of the cloud. Then $r_c$ is the radius of a circle whose projected area is equal to that of the emission at velocity $V_w$. In Table 1A, column (1) gives the central velocity of a 4.2 km s$^{-1}$ window shown in Figure 4. Column (2) gives the characteristic radius for each velocity. The agreement between characteristic radii measured at opposite velocities is excellent and attests to the remarkable symmetry of the flow. The slightly smaller extent of the flow to the southwest may be a consequence of the lower mass density in that direction and our use of a density-sensitive probe. The characteristic radius for the lowest velocity component of the flow is calculated for the area over which $T_R$ exceeds 0.6 K, reflecting the incompleteness of the map at that velocity to a level of 0.2 K.

The velocities and radii listed in Table 1 have been used to estimate characteristic time scales $t(v) = r_c(v)/v$ which are given in years in column (3). The time scale for the lowest velocities still distinguishable in the flow is $t(4) = 4 \times 10^4$ yr, while that for the highest velocity material is less than $t(12) = 3000$ yr. If the flow has been steady, this pattern suggests an evolutionary picture in which the highest velocity portion of the flow decelerates as it sweeps up material during its outward progress. Because the axis of the flow may be inclined by some angle $\gamma$ to the line of sight, the radial velocity $v$ which we measure is related to the space velocity $v'$ by $v = v' \cos \gamma$. Similarly, the characteristic radius $r_c$ is related to actual distance $r_c'$ from the origin of the flow by $r_c = r_c' \sin \gamma$. Therefore the actual crossing time $t'$ is related to the time we estimate $t$ by $t = t' \tan \gamma$. For inclined flows in which the lobes are well separated on the plane of the sky such as NGC 2071, $r_c$ is a good estimator of $r_c'$ but $v$ underestimates $v'$. Therefore the characteristic time $t$ probably overestimates the true time $t'$. This is to some extent compensated by the fact that the flow appears to decelerate.

Clearly the mass at each velocity, and the average mass accumulation rates in the flow at past epochs can now be calculated. The $HCO^+$ abundance derived previously and an extinction temperature of $T_{ex} = 35$ K have been assumed to apply to all material so that total $H_2$ column densities over the areas of the maps of Figure 4 can be calculated. The mass is derived from the product of the area and the column

TABLE 1

THE MOLECULAR FLOW IN NGC 2071

A. VELOCITY ZONE CHARACTERIZATION

| Offset Velocity (km s$^{-1}$) (1) | $r_c$ (cm) (2) | $t$ (yr) (3) | $M$ ($M_\odot$) (4) | $\dot{M}$[a] ($M_\odot$ yr$^{-1}$ (5) | $E$ (ergs) (6) | $P$ (g cm s$^{-1}$) (7) |
|---|---|---|---|---|---|---|
| 21.0 | $<10^{17}$ | $<2 \times 10^3$ | ... | ... | ... | ... |
| 16.8 | $<10^{17}$ | $<3 \times 10^3$ | 0.02: | $>7 \times 10^6$ | $>5 \times 10^{43}$ | $>7 \times 10^{37}$ |
| 12.6 | $1.6 \times 10^{17}$ | $4.0 \times 10^3$ | 0.12 | $3 \times 10^5$ | $2 \times 10^{44}$ | $3 \times 10^{38}$ |
| 8.4 | $3.3 \times 10^{17}$ | $1.2 \times 10^4$ | 0.5 | $4 \times 10^5$ | $4 \times 10^{44}$ | $8 \times 10^{38}$ |
| 4.2 | $4.8 \times 10^{17}$ | $3.7 \times 10^4$ | 1.9 | $5 \times 10^5$ | $3 \times 10^{44}$ | $2 \times 10^{39}$ |

[a] This is the rate at which mass has been swept up by the flow.

B. SPATIAL ZONE CHARACTERIZATION

| $r_c$ (cm) (1) | $M$ ($M_\odot$) (2) | $\langle n \rangle$ (cm$^{-3}$) (3) | $P/V$ (g s cm$^{-2}$) (4) | $E/V$ (ergs cm$^{-3}$) (5) | $\dot{M}V$ ($M_\odot$ yr$^{-1}$) (km s$^{-1}$) (6) | $L$ ($L_\odot$) (7) |
|---|---|---|---|---|---|---|
| $<1.0 \times 10^{17}$ | 0.3 | $1.4 \times 10^4$ | $>4 \times 10^{-14}$ | $>2 \times 10^{-8}$ | $>6 \times 10^{-4}$ | 2.7 |
| $1.6 \times 10^{17}$ | 0.2 | $7 \times 10^3$ | $2 \times 10^{-14}$ | $5 \times 10^{-9}$ | $2 \times 10^{-4}$ | 0.6 |
| $3.3 \times 10^{17}$ | 1.1 | $4 \times 10^3$ | $7 \times 10^{-15}$ | $3 \times 10^{-9}$ | $3 \times 10^{-4}$ | 0.7 |
| $4.8 \times 10^{17}$ | 0.6 | $8 \times 10^2$ | $1 \times 10^{-15}$ | $2 \times 10^{-10}$ | $7 \times 10^{-5}$ | 0.1 |

density and tabulated by velocity in column (4). Because the maps are incomplete to $T_R^* = 0.2$ K, the masses for material at 4 km s$^{-1}$ are lower limits. Average mass accumulation rates for each epoch are listed in column (5). The constancy of these rates at $dM/dt = 4 \times 10^{-5}\ M_\odot$ yr$^{-1}$ in each zone is notable.

From the mass and velocity of the material in each velocity zone, the energy and the momentum for that interval have been tabulated in columns (6) and (7). We have used the measured velocity as the best estimator of the true space velocity necessary to correctly measure momentum and energy. We expect that in the worst case we have underestimated these quantities by a factor of 2. Partly because we are sensitive only to denser parts of the flow. and partly because of the relatively small amount of matter observed at the higher velocities, our estimates for these quantities are considerably lower than Bally's. Over the entire region of the flow mapped, then, $M = 2.5\ M_\odot$, $P = 2 \times 10^{39}$ g cm s$^{-1}$, and $E = 2 \times 10^{45}$ ergs. Most of the momentum and energy are carried in the massive low-velocity component of the flow.

How are the mass, momentum, and energy in the flow distributed through the cloud? To answer this, we divide the cloud into shell-like geometric zones (Table 1B). Unlike the kinetic zones discussed before, these zones are spatially distinct. For convenience, we define the boundaries of these zones at the radii characteristic of the velocity boundaries, listed in column (1) of Table 1B. Thus, the total energy in the innermost zone has contributions from all velocity components in the flow, and in the outermost zone there are contributions only from the low velocity component. The mass (col. [2]), density (col. [3]), momentum (col. [4]), and energy (col. [5]) in these zones are listed normalized to unit volume in Table 1B as computed from equations in the Appendix.

The mean density in the flow, listed in column (3), declines with increasing radius. This decrease might be attributed to either a declining density in the regions responsible for emission, or to a smaller filling factor for the material far from the infrared cluster. However, the strength of the blue emission in the $HCO^+$ $J = 3$–2 line wing remains approximately equal to that in the $J = 1$–0 line to the northeast. This demonstrates that the volume density of the emitting material remains high, and cannot fall as fast as the average density. The rapid fall of the average density in the flow must therefore reflect a falling filling factor. By comparing the volume density determined from the excitation analysis with the average volume density from Table 1, we estimate a volume filling factor of 0.001–0.01, in agreement with the surface filling factor of 0.01–0.05 computed earlier.

Both momentum and energy in the flow are also maximal at the position of the infrared cluster, as expected if it provides the energy to power the flow. The division of the flow into zones of different radii, characterized by different crossing times, allows us to examine the history of the flow. As the flow proceeds outward, sweeping up ambient material, much of the mechanical energy may be converted to unobservable forms of energy. To within a factor of 3, however, the momentum in each resolved shell is constant. Because we have resolved some parts of the flow, each spatial regime that we have defined will have a characteristic momentum and time scale. This allows us to calculate the rate at which momentum was injected into the cloud during past epochs (col. [6]). In the innermost zone of the cloud, $t < 4 \times 10^3$ yr, the values we measure for momentum flux are essentially the same as those we measure in the next zone out ($t = 10^4$ yr). We infer that the flow injection has been fairly stable over this time scale. In the outermost zone, the momentum flux is much lower, perhaps reflecting (1) an evolutionary effect owing to a substantially lower rate of

momentum injection in the era when this material was accelerated or (2) the incompleteness of our maps of this extended zone of lower velocity material.

If we assume that all energy delivered to the gas is transformed into its motion, we can estimate a minimum rate $E_i/t_i$ for each radial zone $i$ with crossing time $t_i$, at which mechanical luminosity must have been delivered to that zone (col. [7]). This rate is highest for the innermost zone, and we take this as good evidence that the source of the flow lies within this zone, and continues to supply energy to the flow. The more modest requirements of the outermost zones undoubtedly reflect the degradation of a good deal of their mechanical energy to other forms of energy.

## V. THE CLOUD CORE: A COLLIMATING DISK?

The dense core of the NGC 2071 molecular cloud envelops the infrared cluster and mediates the interaction between the cluster and the bulk of the matter in the cloud. The location and extent of the core are best studied through the distribution of integrated intensity in the $J = 3$–2 $HCO^+$ line, shown in Figure 8. As we have noted, the intensity of this line does not appear to be appreciably diminished by absorption in foreground material, and so offers a reliable problem of the characteristics of the core. This is an important attribute for a line to have, as the lower transitions of many abundant molecules show the effects of severe absorption evident in Figures 1 and 5. A more subtle absorption shifts the velocity of strongest emission in the $J = 2$–1 line of CS (Bally 1982) or the $J = 1$–0 line of $^{13}CO$ to more positive velocities than those we have measured for $H^{13}CO^+$ or the $J = 3$–2 line of $HCO^+$. The absorption feature is strongest to the northeast of the infrared cluster (Lichten 1982) and distorts maps in the $J = 1$–0 line of CO (Loren 1981*b*) or $HCO^+$ (Fig. 2) so that they mimic the form an inclined disk might take. Although the absorption is much less evident in the CS or $^{13}CO$ lines, the velocity shift of the peak of the emission belies its presence, and maps in those lines are not reliable guides to the characteristics of the dense core. None of these difficulties affect the $J = 3$–2 $HCO^+$ line.

The map of integrated intensity in the $J = 3$–2 $HCO^+$ line, Figure 8, shows no tendency toward elongation in a northwest-southeast direction as do the $J = 1$–0 line of $HCO^+$ (Fig. 2), the $J = 1$–0 CO line, or the $J = 2$–1 line of CS. We conclude that the elongation observed in maps of these latter lines is probably an artifact of the absorption.

In agreement with the CS (Bally 1982), $^{13}CO$ (Lichten 1982), and $H^{13}CO^+$ (Fig. 6) data, a velocity gradient does occur along a northwest-southeast axis, and is similar to that observed on a larger scale through the whole molecular complex (White and Phillips 1981). The gradient is sharper than 4 km $s^{-1}$ $pc^{-1}$ in the vicinity of the cluster (Fig. 6) and an order of magnitude larger than the 0.4 km $s^{-1}$ $pc^{-1}$ observed on the larger scale by White and Phillips (1981). Such a gradient is consistent with a core mass of at least 2 $M_\odot$.

The mass of the dense core can be estimated in several ways. Within a 1.2 (diameter) region observed in the $J = 1$–0 and $J = 3$–2 lines of $H^{13}CO^+$, the mean density can be derived from the line ratio in conjunction with a large velocity gradient analysis of the excitation of $H^{13}CO^+$ (Loren, Wootten, and Peters 1984). From this analysis we find $n(H_2) \sim 4 \times 10^5$ $cm^{-3}$ and $X(H^{13}CO^+) \sim 5 \times 10^{-12}$, assuming for the velocity gradient $dv/dr = \Delta V/2R \sim 5$ km $s^{-1}$ $pc^{-1}$. If this density holds throughout a spherical volume, the molecular mass in the central region is $\sim 50$ $M_\odot$. This must, of course, be reduced if the distribution of matter is clumped or disklike.

An alternative way to estimate the mass of the core uses equation (A11) and the column density of the $J = 3$–2 line of $HCO^+$, equation (A10b), integrating over the area from which emission is observed in Figure 8. In this calculation, we assume that the line is optically thin and that the excitation temperature of the transition is a constant 35 K. A vexing problem for this analysis is the abundance of $HCO^+$ in the core, which may not be as high as in the flow (Wootten, Snell, and Evans 1980). If we choose as a reasonable upper limit $X(HCO^+) \sim 10^{-8}$, the mass of the core is only 0.7 $M_\odot$, unappealingly low for a region which has produced a B5 star of $\sim 6$ $M_\odot$. We might estimate a reasonable lower limit to the abundance from $X(HCO^+) \sim 40\ X(H^{13}CO^+) = 2 \times 10^{-10}$, from which we obtain a total core mass of $\sim 40$ $M_\odot$. Of this mass, half lies within the central beam from which an $H^{13}CO^+$ mass ($< 50$ $M_\odot$) was measured above.

We conclude that the very dense component of the core lies at the position of the infrared cluster. The $J = 3$–2 $HCO^+$ line appears to be free of absorption effects which mask the geometry of the core in other lines. There is no evidence for a disklike geometry in the intensity distribution of that line. The mass of the dense component of the core is less than 50 $M_\odot$.

## VI. IONIZATION LEVELS WITHIN THE FLOW

In the region where the flow collides with dense ambient material, the high temperatures and densities present can change the character of the chemistry of the gas. Reactions which do not occur normally because of energy barriers can significantly alter the relative abundances of some molecules (Elitzur and Watson 1978; Hollenbach and McKee 1980). In particular, Iglesias and Silk (1978) found that the abundance of $HCO^+$ may become depressed in such a region, a fact which Elitzur (1983) attributes to high densities behind the shock. One molecule whose abundance can become enhanced is SiO (Hartquist, Oppenheimer, and Dalgarno 1980). The observations of broad (18 km $s^{-1}$) emission in the $v = 0$, $J = 2$–1 line of SiO (Olofsson *et al.* 1982*b*) toward NGC 2071 (Fig. 1*b*) could constitute evidence for a shock, as does the observations of 2 $\mu$m $H_2$ emission discussed earlier. The central region of NGC 2071 resembles in several respects the central region of the OMC-1 cloud, although in a less spectacular way. Over a 0.4 pc region, the excellent correlation of very broad emission in the wings of the $HCO^+$ lines with molecular hydrogen emission (Bally and Lane, private communication 1983) suggests that these spectral components share a similar origin.

Theoretical calculations of the densities and temperatures required for excitation of the observed $H_2$ emission will also result in $HCO^+$ emission including the $J = 3$–2 line if the molecular abundance is sufficiently high. Our observations of broad emission in the $J = 3$–2 line confirm the presence of regions of density $10^6$ $cm^{-3}$. Our analysis of the $HCO^+$

TABLE 2

COMPARISON OF $HCO^+$ AND CO ABUNDANCES

| Source | Type | $T_{ex}$ (K) | $T_R^*(H^{13}CO^+)$ (K) | $T_R^*(^{13}CO)$ (K) | $\frac{X(H^{13}CO^+)}{X(^{13}CO)}$ | Ref. |
|---|---|---|---|---|---|---|
| L134N | C | 12 | 0.6 | 5.9 | $7 \times 10^{-4}$ | a |
| L1529 | C | 15 | 0.7 | 4.1 | $1 \times 10^{-3}$ | a |
| L63 | C | 17 | 0.4 | 5.5 | $5 \times 10^{-4}$ | a |
| L1551 | C | 18 | 0.7 | 4.5 | $1 \times 10^{-3}$ | a |
| NGC 1333 | C | 25 | 0.6 | 10.1 | $4 \times 10^{-4}$ | a |
| HH 24 | C | 25 | 0.8 | 6.4 | $9 \times 10^{-4}$ | a |
| NGC 2264 | C | 25 | 0.7 | 8.9 | $6 \times 10^{-4}$ | a |
| Ser MC1 | C | 25 | 0.7 | 9.1 | $5 \times 10^{-4}$ | a |
| DR 21 (OH) | C | 25 | 0.8 | 12.3 | $5 \times 10^{-4}$ | a |
| R CrA | C | 29 | 1.9 | 13.0 | $1 \times 10^{-3}$ | a |
| NGC 6914 | C | 30 | 0.4 | 10.0 | $3 \times 10^{-4}$ | a |
| S140 | C | 33 | 0.8 | 8.9 | $6 \times 10^{-4}$ | a |
| OMC 1 | C | 70 | 1.3 | 12.6 | $7 \times 10^{-4}$ | a |
| OMC 1 | HV | 70 | ... | ... | $3 \times 10^{-4}$ | b |
| OMC 1 | NHV | 70 | ... | ... | $3 \times 10^{-3}$ | c |
| NGC 2071 | HV | 35 | ... | ... | $4 \times 10^{-4}$ | |
| Cep A | HV | 35 | ... | ... | $1 \times 10^{-4}$ | d |
| IC 443 | SNR | 50 | 0.6 | 2.0 | $2 \times 10^{-3}$ | e |
| W28 | SNR | 50 | 0.15 | $<0.4$ | $>3 \times 10^{-3}$ | f |
| Mean: | | | | | | |
| C | ... | ... | ... | ... | $7 \pm 3 \times 10^{-4}$ | |
| HV | ... | ... | ... | ... | $3 \pm 2 \times 10^{-4}$ | |
| SNR | ... | ... | ... | ... | $2.4 \pm 0.4 \times 10^{-3}$ | |

NOTE.—In column (2), C indicates measurement refers to cloud core, HV refers to high velocity gas, NHV refers to the northward $HCO^+$ component in OMC 1 (Olofsson *et al.* 1982*a*; Wootten and Loren 1984) and SNR refers to high velocity gas associated with a supernova remnant. For C sources, we assume that $X(H^{13}CO^+)/X(^{13}CO) = X(HCO^+)/X(CO)$. For HV sources, the data refer to $HCO^+$ and $^{13}CO$ measurements, and the data in column (6) assume $X(^{13}CO)/X(CO) = 40$. For SNR sources the data refer to $HCO^+$ and CO measurements.

[a] From Wootten, Loren, and Snell 1982.
[b] From Kuiper, Zuckerman, and Rodriguez-Kuiper 1981.
[c] From Olofsson *et al.* 1982*a*.
[d] From Loren *et al.* 1983.
[e] From DeNoyer and Frerking 1981.
[f] From Wootten 1981.

abundance in the flow suggested that it might be somewhat enhanced in the shocked regions. Because of recent interest in the chemistry of $HCO^+$ in shocked regions (Mitchell and Deveau 1982; Elitzur 1983), and because of the importance of the level of ionization in theories of interstellar shocks which invoked magnetic precursors (Draine 1980), we examine $HCO^+$ abundance in some detail.

The reaction of CO with $H_3^+$ results in the creation of $HCO^+$; the $H_3^+$ derives from the interaction of cosmic rays and $H_2$ in dense regions of a cloud. The ionization level in a cloud results straightforwardly from a measurement of the abundance ratio $X(HCO^+)/X(CO)$ (Wootten, Snell, and Glassgold 1979). Fortunately, these two molecules are easily observed in shocked regions, and the abundance ratio can be determined. Assuming local thermodynamic equilibrium, spatial symmetry of the emission regions, optically thin emission in both lines, and similar velocity profiles for the two lines, the calculation is simple. For $HCO^+$ and CO, these criteria can be met with some confidence in the clouds influenced by the IC 443 (DeNoyer and Frerking 1981) and W28 (Wootten 1981) supernova remnants. For the wing components of the profiles in these clouds we derive the abundance ratio listed in Table 2 using the analytical procedure described by Kuiper, Zuckerman, and Rodriguez Kuiper (1981). In the sources such as NGC 2071, where high-velocity flows are present, the CO line wings can be optically thick (Loren *et al.* 1981). For these sources, we calculate $X(HCO^+)/X(^{13}CO)$, tabulated in column (6) of Table 2. In cloud cores, where unshocked material is likely to dominate the emission, both CO and $HCO^+$ may be optically thick. For these sources we calculate $X(H^{13}CO^+)/X(^{13}CO)$, also tabulated in the sixth column of Table 2, using data from Wootten, Loren, and Snell (1982). To facilitate intercomparison of these abundance ratios, we ignore possible isotopic fractionation effects and assume

$$X(H^{13}CO^+)/X(^{13}CO) = X(HCO^+)/X(CO) = X(HCO^+)/40X(^{13}CO) .$$

The largest values of the ratio are found in clouds near supernova remnants, as expected from the locally enhanced ionization rate in those regions (Elitzur 1983). In the molecular clouds displaying high-velocity flows, the abundance ratio does not appear to be significantly different from that found in quiescent cloud cores. In the "moderately broad line" region of the northern Orion flow, there does appear to be an enhanced $HCO^+$ abundance (Olofsson *et al.* 1982*a*; Wootten and Loren 1984).

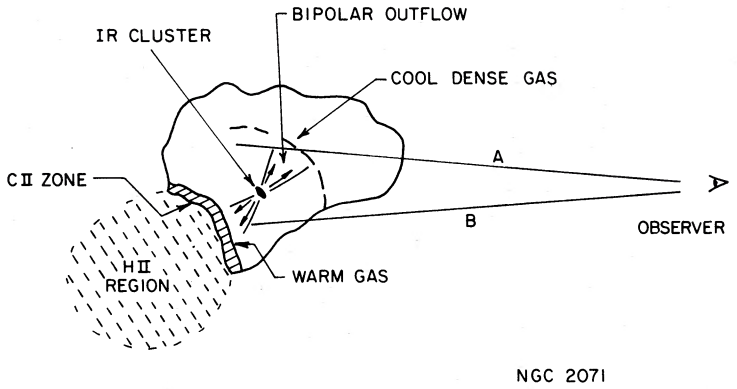


FIG. 10.—A schematic representation of the cloud geometry illustrates important features of the model described in the text

Before proceeding further, consider the consequences of a failure of the LTE assumption. In dense cold regions, excitation temperatures of CO and $HCO^+$ cannot differ by much due to the low temperature and moderate density. In warmer regions, $T_{ex}(CO)$ is expected to be considerably higher than $T_{ex}(HCO^+)$ owing basically to the large difference in radiative deexcitation rates. At high temperature (35 K) and density ($10^5$ cm$^{-3}$), collisional processes again dominate radiative processes and the excitation temperatures of the two species will be similar. A non-LTE calculation of these differences (Wootten, Loren, and Snell 1982) shows that these effects can lower the abundance ratios by a factor of 10 from the numbers listed in column (6) of Table 2.

The electron abundance in the flow can be determined by application of the method of Wootten, Snell, and Glassgold (1979), assuming an ionization rate. If that rate is $\xi = 5 \times 10^{-18}$ s$^{-1}$, the electron abundance in the shocked region is $X_e <= 3 \times 10^{-8}$.

We may also apply this analysis to the core of the NGC 2071 cloud. A detailed analysis of the $H^{13}CO^+$ and $^{13}CO$ excitation in the quiescent cloud results in an $H^{13}CO^+/^{13}CO$ abundance ratio of $6 \times 10^{-4}$. From this we estimate the electron abundance in the unshocked region to be $X_e <= 2 \times 10^{-8}$. We conclude that the observations do not require any appreciable change in ionization levels as the shock accelerates ambient material. Very low ionization levels such as we observe are necessary if material is accelerated by magnetic precursors (Draine 1980).

## VII. THE THERMAL STRUCTURE OF THE NGC 2071 CLOUD

We have illustrated the self-absorption in the $J = 1$–0 $HCO^+$ profile and discussed various aspects of it piecemeal. We now turn our attention to the location of the absorbing material in the cloud, and how it helps to clarify the geometry. Loren and Wootten (1980) attributed the asymmetry in the $J = 1$–0 $HCO^+$ profile to absorption of emission originating in the cloud core by an intervening layer of low-excitation gas, and compared the profile to that of CO. The $J = 1$–0 CO profile (Loren *et al.* 1981) toward NGC 2071, however, lacks the narrow deep feature seen in the $J = 1$–0 $HCO^+$ spectrum. The CO shows only a broad and shallow absorption. Lichten (1982) and Phillips *et al.* (1981) attribute the cold absorbing layer of gas to a component of the local complex of clouds, centered slightly northeast of the dense core. The sharp absorption (Fig. 2) is probably caused by a gradient in excitation temperature within the core material. If so, comparison of the velocities of the self-absorption, procedure in the outer core, and the peak of $H^{13}CO^+$ emission, produced in the core interior, provides a measure of the velocity profile of the gas through the core. Since the self-reversal occurs at a higher velocity than the $H^{13}CO^+$ peak (Fig. 1), the core must then be collapsing. As we have seen, the peak of the $J = 3$–2 line, requiring very high density for excitation, also occurs at lower velocities than the self-absorption, supporting our conclusion.

Sargent *et al.* (1981) have described the temperature distribution of the dust near NGC 2071. They have found that the dust is cooler at the position of the infrared sources than near the H II region to the south. An appealing interpretation of this observation is that the older stars illuminating the H II region are responsible for heating the dense molecular cloud, at least at its southern boundary. The optical appearance of the region (Strom, Strom, and Vrba 1975) suggests that some, if not most, of the obscuring material lies between us and the H II region. An intimate relationship between the H II region and the cloud is suggested by the detection of carbon recombination line emission (van Gorkum, Shaver, and Goss 1979) in its vicinity. We have seen that the outflow has proceeded from the infrared cluster at a fairly constant level over the last $10^4$ years. We suggest that the self-absorption arises in cool material (Fig. 10) located too far from the H II region to have been effectively heated by it or by the newly emerging cluster, an effect compounded by the poor effectiveness of the dust for heating the gas at low density. The cool gas responsible for the self-absorption, blueshifted with respect to center of rest velocities, is being pushed outward by warm gas in the flow. Because of its moderate density and displacement from heating sources in the cloud, it has not yet become as warm as gas in other regions of the cloud. In particular, the origin of an unusual feature of the broad self-absorption in this cloud—viz., it is *blueshifted* rather than *redshifted*—is a natural consequence of the geometry of the cloud. The large column of gas along the line of sight to the redshifted gas lies along the southern edge of the cloud, warmed by the H II region which has formed there. Figure 10 shows a schematic representation of the cloud geometry.

## VIII. SUMMARY

The $HCO^+$ spectrum of the remarkable young star-forming region NGC 2071 has been mapped in detail. Our primary conclusions are:

1. A bidirectional flow of high-velocity gas emanates from a dense ($n \sim 10^6$ cm$^{-3}$) compact core centered on the infrared cluster mapped by Persson *et al.* (1981). No disklike structure is discernible over scales 0.1–1 pc within this core.

2. The highest velocities in the dense component of the flow occur in a limited region near the infrared cluster. Progressively lower velocities are found over progressively larger regions, suggesting that the outflow is decelerated as it evolves, sweeping up material from the surrounding cloud.

3. The highest velocities observed in the flow in the CO line (35 km s$^{-1}$) occur $\sim$0.07 pc northeast of IRS 1, apparently just outside the infrared cluster.

4. The momentum and energy in the flow decrease with increasing velocity and distance from the cluster, while the total mass in the flow increases. The flow appears to consist of dense ($n \sim 10^6$ cm$^{-3}$) clumps of radii less than 0.01 pc.

5. Resolution of several velocity zones in the cloud reveals the historical rate of momentum injection into the flow, which has been constant or slightly increased over the past $10^4$ years. To the extent that this rate is proportional to the luminosity of the central engine, its luminosity evolution has followed the same course.

6. The rotation curve of the cloud has been measured; the velocity discontinuity at the core is not resolved at our highest spatial resolution (0.1 pc), confirming the presence of a central mass concentration.

7. The spatial and velocity extents of blueshifted high-velocity $HCO^+$ emission correlate extremely well with the spatial and velocity extents of $H_2$ emission at 2 $\mu$m, within the uncertainties imposed by interstellar extinction. This result is a natural consequence of the similar excitation requirements (high density) of the two species.

8. The abundance of $HCO^+$ [$X(HCO^+) \sim 10^{-8}$] is not enhanced by a large factor in the shocked region. In this and other respects, the molecular cloud near the infrared cluster in NGC 2071 resembles that near the Kleinmann-Low nebula within OMC-1.

9. The ionization levels deduced from the $HCO^+$ observations in both accelerated and ambient cloud regions are similar. The preshock ion density is sufficiently low that magnetic precursors (Draine 1980) to shocks can contribute to the acceleration of the high-velocity gas.

10. The prominent broad self-absorption feature in the $J = 1$–0 $HCO^+$ profiles originates in cool material accelerated toward us by the expansion.

11. Optically thick $HCO^+$ at low excitation temperatures which absorbs radiation from the cloud core in the $J = 1$–0 line, is too cool to absorb an appreciable fraction of the radiation in the $J = 3$–2 line. The higher transitions of abundant molecules therefore offer more direct probes of material in the dense core than do the lower transitions.

In part because we observe it in a fortuitous geometrical configuration, in part because we observe it at a fortuitous developmental stage, the NGC 2071 region illustrates a remarkably clear scene in the early life of a star-bearing molecular cloud. The geometry of the region of most recent star formation has allowed us to read, in the progress of the outflow, the history of the last 10 millenia of its evolution. This record chronicles the constant or gradually increasing rate of momentum injection as the new stars evolve. Coincidentally, similar dynamic and thermal time scales in this cloud have left us with a history of the thermal evolution of the cloud, too. This record, partially deciphered by Sargent *et al.* (1981), tells of a more ancient star-forming event which initially heated the nearby portions of the cloud. This process has continued through the more recent events, and finally only the cool gas pushed toward us by the flow remains to document its progress. Owing to its special circumstances, NGC 2071 has provided us with the tools necessary to determine the evolutionary status of other star-bearing molecular clouds, which we will discuss in subsequent papers.

The course of this study was influenced by discussions during the Workshop on Star Formation held at the University of California at Santa Cruz in 1979. Discussions with G. Knapp, J. Bally, R. Snell, A. Sargent, T. G. Phillips, and S. Lichten have been invaluable. This research has been supported in part by NSF grants 79-16815 to OVRO, and AST81-16403 to The University of Texas at Austin, and by the Swedish Natural Science Research Council. The MWO observations were taken with a receiver constructed by N. Erickson of the University of Massachusetts. Receiver development there is supported by a grant from the National Science Foundation. A. W. is particularly grateful to the Dudley Observatory for a Dudley Award to accomplish a portion of this research, and to Stockholm Observatory for their hospitality during another portion of this work.

## APPENDIX

In this appendix we elaborate on the method we have used to derive the parameters of the flow.

The optical depth at a frequency $v$ is defined in terms of the total absorption coefficient $\kappa_v$ along the line of sight $dl$ by

$$d\tau = -\kappa_v dl . \tag{A1}$$

But this total absorption coefficient is just the product of the absorption cross section per particle, $s_v$, times the number of particles per unit volume in the lower state $n_j$. Integrating along a line of sight and over an average frequency profile $\bar{\varphi}$, we obtain

$$\tau = N_j s \bar{\varphi} , \tag{A2}$$

where $s$ is the frequency integral of $s_v$ and $N_j$ is $n_j$ integrated along the line of sight. Integrating over the line, we then have

$$\tau = \int \tau_v dv = N_j s \bar{\varphi} . \tag{A3}$$

Now the intensity profile is

$$I(\nu_{jk})\int \kappa_\nu \, d\nu = \frac{h\nu_{jk}}{c}(n_j B_{jk} - n_k B_{kj})I(\nu_{jk}) = I(\nu_{jk})n_j s \tag{A4}$$

and the source function $s$ is

$$s = \frac{h\nu_{jk}}{c} B_{jk}\left(1 - \frac{n_k}{n_j}\frac{g_j}{g_k}\right).$$

Assuming LTE allows us to write

$$s = \frac{g_k}{g_j}\frac{h\nu_{jk}}{c}\frac{c^3}{8\pi h\nu_{jk}{}^3} A_{kj}\left[1 - \exp\left(-\frac{h\nu_{jk}}{kT_{ex}}\right)\right], \tag{A5}$$

where we have substituted the usual relationships between the Einstein $B$ and $A$. Then

$$\tau = N_j \frac{c^2 \bar{\varphi} A_{kj} g_k}{8\pi\nu^2 g_j}\left[1 - \exp\left(-\frac{h\nu_{jk}}{kT_{ex}}\right)\right]. \tag{A6}$$

The transfer equation is

$$T_R = f[J(T_{ex}) - J(T_{bg})](1 - e^{-\tau}), \tag{A7}$$

where $J(T_{ex}) = (h\nu/k)[\exp(h\nu/kT_{ex}) - 1]^{-1}$, $T_{bg}$ is the temperature of the universal background radiation, $f$ is the filling factor, and $\tau$ is the optical depth. For small $\tau$ and assuming $f = 1$,

$$T_R = J(T_{ex})\tau \sim T_{ex}\,\tau\ ; \tag{A8}$$

and for large $\tau$,

$$T_R = J(T_{ex}) \sim T_{ex}\ . \tag{A9}$$

To obtain the column density in all states of the absorbing molecule, we assume that the rotational levels are populated in LTE and that the intrinsic profile is Gaussian. For the $J = 1$–$0$ line of $HCO^+$ we obtain

$$N(HCO^+)_{1\to 0} = \frac{3.45 \times 10^{11} T_R{}^* \Delta v_{FWHM}}{(1 - e^{-4.2/T_{ex}})}\ ; \tag{A10a}$$

and for the $J = 3$–$2$ line the column density is given by

$$N(HCO^+)_{3\to 2} = \frac{8.9 \times 10^{10} T_R{}^* \Delta v_{FWHM}}{(1 - e^{-12.6/T_{ex}})(e^{-12.6/T_{ex}})}\ ; \tag{A10b}$$

where a dipole moment of 3.3 debyes has been used. The total mass in an annulus between radii $r_{i-1}$ and $r_i$, of area $A_i$, is

$$M_i = m(H_2)\int_{r_{i-1}}^{r_i}\int_{\text{wings}} N(H_2)T_R(r, v)/T_{ex}\, dv dr\ ; \tag{A11}$$

and the momentum and energy are

$$P_i = m(H_2)\int_{r_{i-1}}^{r_i}\int_{\text{wings}} N(H_2)T_R(r, v)v/T_{ex}\, dv dr\,, \tag{A12}$$

$$E_i = \frac{1}{2}\, m(H_2)\int_{r_{i-1}}^{r_i}\int_{\text{wings}} N(H_2)T_R(r, v)\frac{v^2}{T_{ex}}\, dv dr\,, \tag{A13}$$

from which the numbers in Table 1 were calculated.

## REFERENCES


Allen, D. A., Barton, J. R., and Gillingham, P. R. 1980, *M.N.R.A.S.*, **192**, 805.
Bally, J. 1982, *Ap. J.*, **261**, 558.
Bally, J., and Lane, A. 1982, *Ap. J.*, **257**, 612.
Bally, J., and Predmore, R. 1983, *Ap. J.*, **265**, 778.
Barral, J. F., and Cantó, J. 1981, *Rev. Mexicana Astr. Ap.*, **5**, 101.
Campbell, P. D. 1978, *Pub. A.S.P.*, **90**, 262.
DeNoyer, L. K., and Frerking, M. A. 1981, *Ap. J. (Letters)*, **246**, L37.
Draine, B. T. 1980, *Ap. J.*, **241**, 1041.
Elitzur, M. 1983, *Ap. J.*, **167**, 174.
Elitzur, M., and Watson, W. D. 1978, *Ap. J. (Letters)*, **222**, L141.
Evans, N. J., II, Beckwith, S., Brown, R. L., and Gilmore, W. 1979, *Ap. J.*, **227**, 450.
Genzel, R., and Downes, D. 1979, *Astr. Ap.*, **72**, 234.
Gilmore, W. 1980, *A.J.*, **85**, 912.
Hartquist, T. W., Oppenheimer, M., and Dalgarno, A. 1980, *Ap. J.*, **236**, 182.
Harvey, P. M., Campbell, M. F., Hoffman, W. F., Thronson, H. A., Jr., and Gatley, I. 1979, *Ap. J.*, **229**, 990.
Hollenbach, D., and McKee, C. F. 1979, *Ap. J. Suppl.*, **41**, 555.
Iglesias, E. R., and Silk, J. 1978, *Ap. J.*, **226**, 851.
Johansson, L. E. B., Hoglund, B., Winnberg, A., Nguyen-Q-Rieu, and Goss, W. M. 1974, *Ap. J.*, **189**, 455.

Knapp, G. R., Phillips, T. G., Huggins, P. J., and Redman, R. O. 1981, *Ap. J.*, **250**, 175.
Kuiper, T. B. H., Zuckerman, B., and Rodriguez Kuiper, E. N. 1981, *Ap. J.*, **251**, 88.
Kutner, M. L., and Ulich, B. L. 1981, *Ap. J.*, **250**, 341.
Kwan, J., and Scoville, N. Z. 1976, *Ap. J.* (*Letters*), **210**, L39.
Lada, C. J. 1976, private communication.
Lada, C. J., and Harvey, P. M. 1981, *Ap. J.*, **245**, 58.
Lichten, S. M. 1982, *Ap. J.*, **253**, 593.
———. 1983, unpublished Ph.D. dissertation, Caltech.
Loren, R. B. 1977, *Ap. J.*, **215**, 129.
———. 1981*a*, *A.J.*, **86**, 69.
———. 1981*b*, *Ap. J.*, **249**, 550.
Loren, R. B., Plambeck, R. L., Davis, J. H., and Snell, R. L. 1981, *Ap. J.*, **245**, 495.
Loren, R. B., Sandqvist, Aa., Wootten, A., Friberg, P., and Hjalmarson, Å. 1983, *Ap. J.*, submitted.
Loren, R. B., and Wootten, H. A. 1980, *Ap. J.*, **242**, 568.
Loren, R. B., Wootten, A., and Peters, W. L., III. 1984, in preparation.
Mayer, C. E., Davis, J. H., Peters, W. L., III, and Vogel, W. J. 1983, *IEEE Trans., Antennas Propagat.*, **IM-32**, 102.
Mitchell, G. F., and Deveau, T. J. 1982, *Ap. J.*, **253**, 154.
Mundy, L. 1982, private communication.
Olofsson, H., Elldér, J., Hjalmarson, Å., and Rydbeck, G. 1982*a*, *Astr. Ap.*, **113**, L18.
Olofsson, H., Johansson, L. E. B., Hjalmarson, Å., and Nguyen-Quang-Rieu. 1982*b*, *Astr. Ap.*, **107**, 128.
Pankonin, V., Winnberg, A., and Booth, R. S. 1977, *Astr. Ap.*, **58**, L25.
Persson, E., Geballe, T. R., Simon, T., Londale, C. J., and Baas, F. 1981, *Ap. J.* (*Letters*), **251**, L85.
Phillips, T. G., Knapp, G. R., Huggins, P. J., Werner, M. W., Wannier, P. G., Neugebauer, G., and Ennis, D. 1981, *Ap. J.*, **245**, 512.
Plambeck, R., Snell, R., and Loren, R. 1983, *Ap. J.*, **266**, 321.
Rodríguez, L. F., Ho, P. T. P., and Moran, J. M. 1980, *Ap. J.* (*Letters*), **240**, L149.
Sandqvist, Aa., Loren, R. B., Wootten, A., Friberg, P., and Hjalmarson, Å. 1982*a*, in *The Scientific Importance of Submillimetre Observations.*, ed. T. de Graauw and T. D. Guyenne (ESA SP-189), p. 131.
Sandqvist, Aa., Wootten, A., Loren, R. B., Friberg, P., and Hjalmarson, Å. 1982*b*, in *Regions of Recent Star Formation.*, ed. R. S. Roger and P. E. Dewdney (Drodrecht: Reidel), p. 307.
Sargent, A. I., van Duinen, R. J., Fridlund, C. V. M., Nordh, H. L., and Aalders, J. W. G. 1981, *Ap. J.*, **249**, 607.
Sastry, K. V. L. N., Herbst, E., and DeLucia, F. C. 1981, *J. Chem. Phys.*, **75**, 4169.
Snell, R. L., Loren, R. B., and Plambeck, R. L. 1980, *Ap. J.* (*Letters*), **239**, L17.
Strom, K. M., Strom, S. E., and Vrba, F. J. 1975, *A.J.*, **81**, 308.
Ulich, B. L., and Haas, R. W. 1976, *Ap. J. Suppl.*, **30**, 247.
van Gorkum, J. H., Shaver, P. A., qnd Goss, W. M. 1979, *Astr. Ap.*, **76**, 1.
White, G. J., and Phillips, J. P. 1981, *M.N.R.A.S.*, **194**, 947.
Wootten, A. 1981, *Ap. J.*, **245**, 105.
Wootten, A., and Loren, R. B. 1984, in preparation.
Wootten, A. Loren, R. B., and Snell, R. L. 1982, *Ap. J.*, **255**, 160.
Wootten, A., Snell, R. L., and Evans, N. J., II. 1980, *Ap. J.*, **240**, 532.
Wootten, A., Snell, R. L., and Glassgold, A. E. 1979, *Ap. J.*, **234**, 876.
Zuckerman, B., Kuiper, T. B. H., and Rodriguez Kuiper, E. N. 1976, *Ap. J.* (*Letters*), **209**, L137.

PER FRIBERG and ÅKE HJALMARSON: Onsala Space Observatory, S-43900 Onsala, Sweden

R. B. LOREN: Millimeter Wave Observatory, McDonald Observatory, Fort Davis, TX 79734

AA. SANDQVIST: Stockholm Observatory, S-13300 Saltsjobaden, Sweden

A. WOOTTEN: National Radio Astronomy Observatory, Edgemont Road, Charlottesville, VA 22901